6.2

UNMANNED AERIAL VEHICLE MEASUREMENTS OF THE ATMOSPHERIC SURFACE LAYER TURBULENCE EVOLUTION DURING TOTAL SOLAR ECLIPSE

Caleb A. Canter, Michael P. Sama, Suzanne W. Smith, and Sean C. C. Bailey*
University of Kentucky, Lexington, Kentucky

1 INTRODUCTION

During a solar eclipse the insolation change is more rapid than in the evening and morning, making this astronomical event an interesting one from a meteorological perspective. Hence, there have been numerous studies reporting meteorological measurements made during both partial and total eclipse conditions. Generally, the phase of the eclipse can be described using the terms first, second, third and fourth contact which refer to the times at which the eclipse starts, totality starts, totality ends, and the eclipse ends, respectively. For a partial eclipse, there is no second and third contact and instead one uses the time of maximum obscuration to separate the phases of the eclipse.

Except for a few remote sensing experiments Kapoor *et al.* (1982); Eaton *et al.* (1997); Girard-Ardhuin *et al.* (2003); Amiridis *et al.* (2007), observations of atmospheric surface layer properties have been limited to surface observations. Generally, the decrease in insolation which occurs during the eclipse is accompanied by a corresponding decrease in temperature Bala Subrahamanyam *et al.* (2011); Gray & Harrison (2016); Edward (2000). The minimum temperature occurs after third contact, or maximum obscuration, with time lags typically on the order of 10 to 20 minutes reported Winkler *et al.* (2001); Foken *et al.* (2001); Founda *et al.* (2007) with a lag of 30 minutes reported over the Antarctic Takao *et al.* (2009) attributed to the reduced insolation at this location. Observations of the surface winds indicate less consistent behavior. Although some studies report a decrease in wind corresponding to the decrease in temperature Krishnan *et al.* (2004); Bala Subrahamanyam *et al.* (2011); Gray & Harrison (2016), others note no change in the surface winds Girard-Ardhuin *et al.* (2003).

One of the difficulties in interpreting surface winds, in particular their decrease and change in direction, is the potential suppression of turbulence which may occur due to re-stabilization of the atmospheric surface layer which could occur as the surface cools relative to the air Girard-Ardhuin *et al.* (2003); Gray & Harrison (2016). Most studies that report on surface layer stability indicate that there is an increase in stability of the boundary layer, although both fully stable conditions Amiridis *et al.* (2007); Winkler *et al.* (2001); Eaton *et al.* (1997); Antonia *et al.* (1979) and marginally unstable conditions Gorchakov *et al.* (2008); Bala Subrahamanyam *et al.* (2011); Kastendeuch *et al.* (2016); Amiridis *et al.* (2007) have been reported to occur during the eclipse. When stable conditions are reported, they persist for as long as 45 minutes after maximum obscuration Foken *et al.* (2001); Eaton *et al.* (1997); Girard-Ardhuin *et al.* (2003).

The study reported here takes advantage of recent advancements in unmanned aerial vehicle (UAV) technology and employed multiple, instrumented, UAVs in the atmospheric surface layer to resolve the dynamics of the turbulence and coherent motions as they respond to the rapid insolation changes which occur during a total eclipse. The study was conducted in Russellville, Kentucky, USA (36.797326° latitude, -86.812341° longitude) during the total eclipse of August 21, 2017. In addition to being within the path of totality, at this location, first contact initiated at 11:58, when the insolation during the uninterrupted diurnal cycle is at a maximum, and hence also the impact of the eclipse. Second contact occurred at 13:26, third contact at 13:28, and fourth contact at 14:53. Note all times provided are in local time, Central Daylight Time (CDT). On this day, the sky was virtually cloudless, further maximizing the response of the atmospheric surface layer to the eclipse.

2 METHODS

The measurements were conducted at the Russellville airport ($36°$47'50.0"N, $86°$49'02.1"W, 210 m above sea level) located 6 km to the southeast of Russellville, Kentucky, USA. The measurement area is shown in Fig. 1. The airport is surrounded by heterogeneous land use, mostly consisting of farmland with associated scattered stands of trees and ponds within a 5

* *Corresponding author address:*
Sean C. C. Bailey, Dept. of Mechanical Engineering, Univ. of Kentucky, Lexington, KY, 40506; email: sean.bailey@uky.edu

km radius. A larger stand of trees was located 1.5 km to the north of the airport.

Mean winds for the day reported in METAR data from the nearby Bowling Green airport were 1.4 m/s from the SSW, with mean temperatures of 27° C, sea level pressure of 102.0 kPa, mean humidity of 71%.

Measurements were conducted between approximately 9:00 CDT and 15:00 CDT using 5 different types of systems. These systems consisted of two BLUECAT5 fixed-wing unmanned aerial vehicles (UAVs), one SOLO rotary wing vehicle, a portable weather station, ground temperature sensors, and a sonic anemometer. The locations of each system is indicated in Fig. 1.

Two BLUECAT5 aircraft were flown simultaneously at 50 m and 100 m AGL. Each flight consisted of repeatedly traversing the same 800 m long straight line transects at 20 m/s, indicated on Fig. 1, with typically 40 transects made in alternating directions with 50 s between each transect. After approximately 40 minutes of flight time, the aircraft were recovered, data downloaded and batteries changed, making the aircraft ready for the next flight. Five of these multi-aircraft flights were conducted, approximately once per hour, between 10:20 CDT and 14:45 CDT.

The portable weather station logged continuously at 1 Hz from 9:20 CDT to 14:57 CDT. Ground temperature data was logged at 1 Hz between 9:08 CDT and 15:19 CDT. The sonic anemometer was mounted on a 7 m tower with data logged continuously from 9:33 CDT to 15:00 CDT at 100 Hz.

The SOLO rotorcraft was flown between 10:23 CDT and 14:39 CDT. This aircraft was operated above the sonic anemometer, flying vertical ascents and descents at 2 m/s between 10 m and 100 m. Up to 10 ascent/descent combinations would be flown in a single flight before the aircraft's batteries required changing. Once the batteries were changed, the aircraft was returned to flight. Fifteen of these flights were flown during the measurement day, with times between flight altered depending on battery availability and charge rates, with most flights separated by less than 5 minutes but flights 8 and 9 separated by 37 minutes.

3 RESULTS

3.1 *Solar Radiation*

These boundary conditions to the atmosphere are reflected in the information recovered from the ground sensors during the day of the eclipse. The clearest indicator of the phase eclipse is the measured solar radiation shown in Fig. 2. For the cloudless, summer morning of the eclipse, the solar radiation increases gradually with the sun's elevation at approximately 5 W/(m^2 min) during the uninterrupted diurnal evolution. The impact of the eclipse, however, is readily evident in an almost linear decrease in measured solar radiation from a peak of 850 W/m^2 at first contact to 0 W/m^2 at second contact at a rate of 10 W/(m^2 min). There is no measured radiation during totality, but there is a 10 W/(m^2 min) linear recovery from third contact to fourth contact.

For convenience, we will divide the atmospheric surface layer processes into six different phenomenological regimes. Regime I is the unaffected evolution of the boundary layer. At first contact, Regime II initiated. We define this regime as being one where all heat fluxes are close to being in balance, resulting in steady state temperature conditions for both the air and surface. Regime II lasted for approximately 30 minutes before the solar radiation dropped below the combined rate of conduction and turbulent flux away from the surface, and the initiation of Regime III. Lasting until second contact, Regime III is characterized by a strong decrease in both soil and air temperatures.

Regime IV occurred between second and third contact and encompasses totality. Within this regime the solar radiation was zero, and the the ground surface had cooled to become equal, or near equal, to the air temperature.

Regime V is defined around the region when when the soil and air temperature were at minimum, with both the soil and air temperature reaching a minimum at 13:39, 11 minutes after third contact. At this time, the solar radiation had increased back to approximately 15% of its first contact value.

We define Regime VI as the recovery regime.

3.2 *Atmospheric Surface Layer Structure*

The measured solar radiation suggests a very dynamic process could be occurring during the eclipse, with changes observed in all measured properties at the surface. However, without measurements of these properties at higher altitudes, we can only infer the source of many of these changes. The advantages of unmanned aerial vehicles become evident in their ability to interrogate a wider range of altitudes within the the surface layer than can be accessed via ground instrumentation. With this information, we can connect the regimes established during the discussion of boundary conditions to boundary layer dynamics, most notably through the formation and suppression of coherent structures throughout the eclipse evolution. To make this connection, we present isocontours of temperature and potential temperature measured during each flight as a function of altitude and time in Fig.

3a-b.

Regime I was characterized by the development of mixed layer conditions typical of a cloudless day. These convective structures, most clearly observed in the temperature fields, appear as vertical perturbations which get stronger as the temperature difference between the air and surface increases. Although their presence is most easily visualized in the temperature field, the potential temperature fields reveal the vertical scale of the structures, with many of them extending throughout the domain, and several structures detached from the surface also observed.

These mixed layer conditions continued in Regimes II and III, however the convective structures are strongest during Regime II due to the maximization of temperature difference between the air and surface. As the ground and air cooled within Regime III the convective behavior weakened, but mixed layer conditions persisted until second contact.

During Regime IV, the convective motions were completely suppressed and stable conditions began to form. This stabilization is reflected in the mean potential temperature profile, which shows a positive temperature gradient formed.

Regime V was the most dynamic in the surface layer and is by far the most interesting regime. Corresponding to this regime is the formation of a temperature inversion Above this stable layer, the wind speed reduced slightly, but the mean flow largely remained unaffected by the changes at the surface. The stable layer grew in time, reaching approximately 50 m in height at 13:45, when the ground temperature and near-surface air temperature were at a minimum. At this time, there is evidence that Kelvin-Helmholtz waves formed in the temperature field, and to a lesser extent the wind field (not shown), at the interface between the stable layer and the residual layer above it. As the surface warmed towards the end of the regime, the temperature inversion retreated toward the surface and neutral conditions returned, signaling the end of Regime V. Thus, Regime V represents the formation of a short-lived nocturnal layer, lasting 45 minutes after third contact.

During Regime VI, convective structures were once again evident, driven by the increased thermal gradients at the surface, and increasing in strength towards fourth contact.

3.3 *Effect on Turbulence*

The above discussion illustrates the changes which were observed in the large-scale dynamics within the surface layer throughout Regimes I to VI. Now, we examine how these dynamics influenced the turbulence, as reflected in some of the turbulence statistics measured by the fixed-wing UAVs flying at 50 m and 100 m and shown in Fig. 4. Where possible, we also include the same statistics measured at 7 m by the tower-mounted sonic anemometer.

For most of the day, as evidenced in Fig. 3, the surface layer exhibited classical mixed layer behavior, with transport and mixing driven by large-scale convective eddies. This buoyant forcing can be quantified by the buoyant production term of the turbulent kinetic energy budget, shown in Fig. 4a. Although it oscillated significantly due to large-scale mixing events, the buoyant production displayed a general increase in time within Regime I, producing a corresponding increase in turbulent kinetic energy. The turbulent kinetic energy, which is shown in Fig. 4b, provides a concise quantification of the intensity of the turbulence, and increased within Regime I, three- to four-fold at 7 m, 50 m and 100 m over an hour long period from 10:30 to 11:30 as the convective eddies observed in Fig. 3a increase in intensity and introduce additional shearing and turbulence production.

During Regime II the conditions at the surface were in an approximately steady state and, although the buoyant production measured at 50 m and 100 m appears to have decreased, the corresponding turbulent kinetic energy remained near its maximum values. However, the measurements at 7 m suggest that the turbulent kinetic energy at this height may have begun to decrease.

The decrease in solar radiation, and corresponding reduction in convective activity during Regime III, was quite dramatic. This resulted in the buoyant production at 50 m and 100 m becoming completely damped out by Regime IV and the initiation of totality. The turbulent kinetic energy experienced a corresponding decrease and is near zero by Regime IV. Damped by the stable layer forming in Regime V, the Buoyant production and turbulent kinetic energy remain near zero until Regime VI, at which point they begin to recover as the solar radiation increases back to non-eclipse levels.

Given that the stable layer forming during Regime V forms within the lowest 50 m (Fig. 3), this is the depth at which one would expect most of the turbulence to be damped. Therefore the reduction in turbulence at 50 m and 100 m is attributed to the lack of a production mechanism coupled with a high rate of dissipation. The residual layer conditions which formed above the stable layer were well mixed, and as a result, lack the mean temperature and humidity gradients required for buoyant and mechanical production of turbulence. Without a mechanism for sustaining its energy, the turbulence dissipation took over, causing the turbulent kinetic energy to rapidly decay.

4 DISCUSSION AND CONCLUSIONS

In summary, these measurements provide a unique view of the atmospheric surface layer processes during a solar eclipse and thereby present a much more complete picture of the evolution of these processes during the rapid decrease and increase of insolation which occurs. Although these types of observations are not necessarily limited to UAVs, the use of these systems for these measurements enabled detailed measurements of a transient phenomena occurring within the lower 100 m of the boundary layer. Prior observations of the atmospheric surface layer processes were made via surface installations, or via remote sensing measurements, resulting in a gap between the surface and the minimum altitude resolved by the remote sensing instruments.

Using the boundary conditions measured at the surface, we were able to identify six different regimes of behavior during the eclipse. These regimes generally describe the typical diurnal evolution, damping of turbulent behavior, formation of a stable nocturnal layer, and recovery back to the typical diurnal evolution. Note that which regimes are observed at a particular location can be expected to vary depending on several factors including: the time of day of the eclipse; time of the year; geography; and synoptic scale weather. These factors will influence cloud cover, and relative surface and near-surface air temperature which will produce different phenomenology and surface observations.

During the measurement campaign reported here, the conditions were optimal for observing significant transient behavior, allowing us to observe the formation and decay of large-scale convective events as the temperature gradients near the surface reduced between first and second contact. A temperature inversion and 50 m deep stable layer formed following totality, which thinned as the solar radiation increased and warmed the surface.

The existence of this layer results in observations made at ground level being very different from observations made at altitude. For example, this layer results in the calming of the wind and the cooling of the air, phenomena which have been assumed to be linked to the formation of a nocturnal layer, but here we see via direct observation that this behavior is limited to the lowest 50 m of the atmospheric surface layer and associated with the suppression of mixing inducing convective eddies. The formation, or lack thereof, of such a stable layer which may form during an eclipse explains some of the confusion surrounding the eclipse wind behavior, as its suppression of convective events and turbulence will confound observations of wind conditions near the surface. Conversely, the properties of the turbulence above the stable layer are influenced by the elimination of production mechanisms at the surface, resulting in a rapid decay of the turbulence throughout the measurement domain.

References

AMIRIDIS, V., MELAS, D., BALIS, D. S., PAPAYANNIS, A., FOUNDA, D., KATRAGKOU, E., GIANNAKAKI, E., MAMOURI, R. E., GERASOPOULOS, E. & ZEREFOS, C. 2007 Aerosol lidar observations and model calculations of the planetary boundary layer evolution over greece, during the march 2006 total solar eclipse. *Atmospheric Chemistry and Physics* **7** (24), 6181–6189.

ANTONIA, R. A., CHAMBERS, A.J., PHONG-ANANT, D., RAJAGOPALAN, S. & SREENIVASAN, KATEPALLI 1979 Response of atmospheric surface-layer turbulence to a partial solar eclipse. *JOURNAL OF GEOPHYSICAL RESEARCH-OCEANS AND ATMOSPHERES* **84** (NC4), 1689–1692.

BALA SUBRAHAMANYAM, D., ANUROSE, T. J., MOHAN, MANNIL, SANTOSH, M., KIRAN KUMAR, N. V. P., SIJIKUMAR, S., PRIJITH, S. S. & ALOYSIUS, MARINA 2011 Atmospheric surface-layer response to the annular solar eclipse of 15 january 2010 over thiruvananthapuram, india. *Boundary-Layer Meteorology* **141** (2), 325.

EATON, F. D., HINES, J. R., HATCH, W. H., CIONCO, R. M., BYERS, J., GARVEY, D. & MILLER, D. R. 1997 Solar eclipse effects observed in the planetary boundary layer over a desert. *Boundary-Layer Meteorology* **83** (2), 331–346.

EDWARD, HANNA 2000 Meteorological effects of the solar eclipse of 11 august 1999. *Weather* **55** (12), 430–446.

FOKEN, THOMAS, WICHURA, BODO, KLEMM, OTTO, GERCHAU, JÖRG, WINTERHALTER, MARTIN & WEIDINGER, TAMÁS 2001 Micrometeorological measurements during the total solar eclipse of august 11, 1999. *Meteorologische Zeitschrift* **10** (3), 171–178.

FOUNDA, D., MELAS, D., LYKOUDIS, S., LISARIDIS, I., GERASOPOULOS, E., KOUVARAKIS, G., PETRAKIS, M. & ZEREFOS, C. 2007 The effect of the total solar eclipse of 29 march 2006 on meteorological variables in greece. *Atmospheric Chemistry and Physics* **7** (21), 5543–5553.

GIRARD-ARDHUIN, FANNY, BÉNECH, B., CAMPISTRON, B., DESSENS, J. & JACOBY-KOALY, S. 2003 Remote sensing and surface observations of the response of the atmospheric boundary layer to a solar eclipse. *Boundary-Layer Meteorology* **106** (1), 93–115.

GORCHAKOV, G. I., KADYGROV, E. N., KORTUNOVA, Z. V., ISAKOV, A. A., KARPOV, A. V., KOPEIKIN, V. M. & MILLER, E. A. 2008 Eclipse effects in the atmospheric boundary layer. *Izvestiya, Atmospheric and Oceanic Physics* **44** (1), 100–106.

GRAY, S. L. & HARRISON, R. G. 2016 Eclipse-induced wind changes over the british isles on the 20 march 2015. *Philosophical Transactions of the Royal Society of London A: Mathematical, Physical and Engineering Sciences* **374** (2077).

KAPOOR, RAMESH K., ADIGA, B. B., SINGAL, S. P., AGGARWAL, S. K. & GERA, B. S. 1982 Studies of the atmospheric stability characteristics during the solar eclipse of february 16, 1980. *Boundary-Layer Meteorology* **24** (4), 415–419.

KASTENDEUCH, PIERRE P., NAJJAR, GEORGES, COLIN, JRME, LUHAHE, RAPHAL & BRUCKMANN, FRANCIS 2016 Effects of the 20 march 2015 solar eclipse in strasbourg, france. *Weather* **71** (3), 55–62.

KRISHNAN, PRAVEENA, KUNHIKRISHNAN, P. K., MURALEEDHARAN NAIR, S., RAVINDRAN, SUDHA, RAMACHANDRAN, RADHIKA, SUBRAHAMANYAM, D. B. & VENKATA RAMANA, M. 2004 Observations of the atmospheric surface layer parameters over a semi arid region during the solar eclipse of august 11th, 1999. *Journal of Earth System Science* **113** (3), 353–363.

TAKAO, KAMEDA, KOJI, FUJITA, OKIMASA, SUGITA, NAOHIKO, HIRASAWA & SHUHEI, TAKAHASHI 2009 Total solar eclipse over antarctica on 23 november 2003 and its effects on the atmosphere and snow near the ice sheet surface at dome fuji. *Journal of Geophysical Research: Atmospheres* **114** (D18).

WINKLER, PETER, KAMINSKI, UWE, KÖHLER, ULF, RIEDL, JOHANN, SCHROERS, HANS & ANWENDER, DORIS 2001 Development of meteorological parameters and total ozone during the total solar eclipse of august 11, 1999. *Meteorologische Zeitschrift* **10** (3), 193–199.

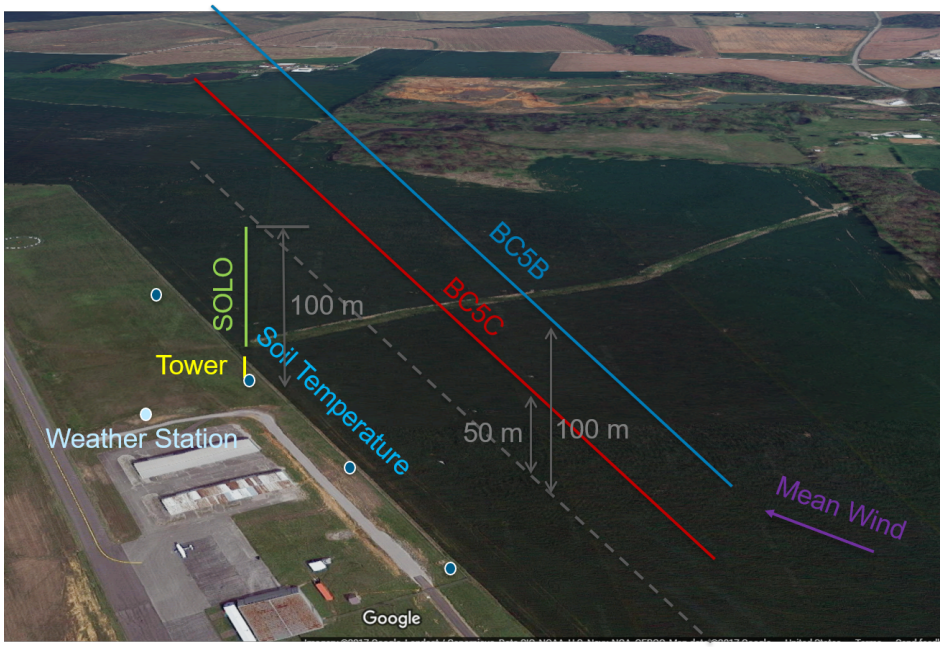

Figure 1: Aerial image of Russellville airport showing locations of different measurement stations.

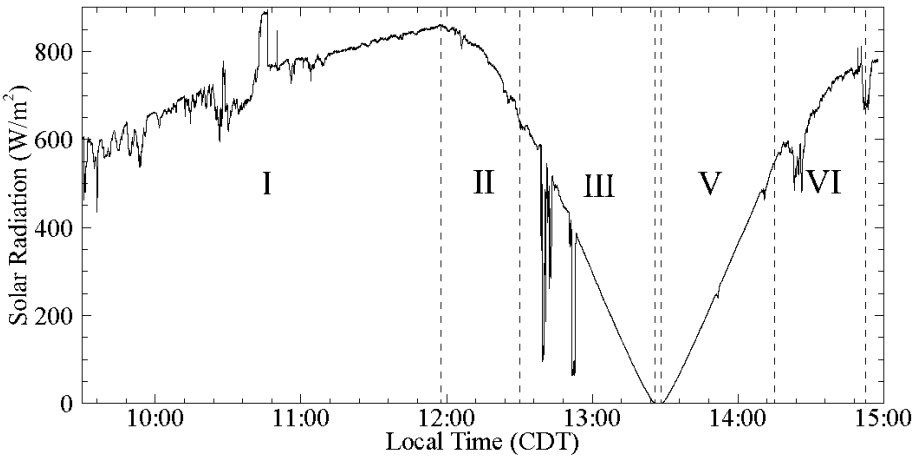

Figure 2: Solar radiation measured from 9:30 CDT to 15:00 CDT. Vertical lines indicate boundaries between regimes with regimes identified by roman numerals.

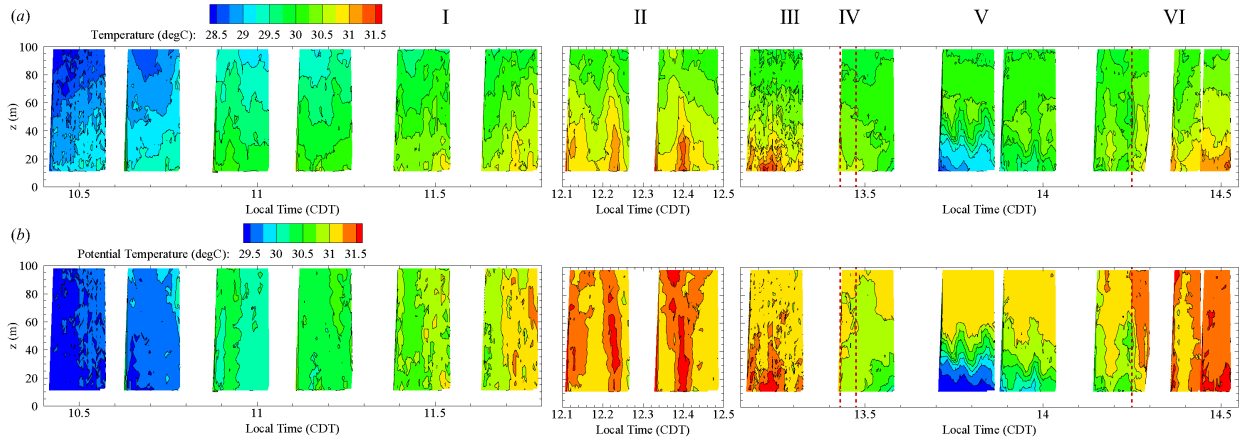

Figure 3: Time evolution of large-scale features of the atmospheric surface layer measured between 10 m and 100 m: (a) Isocontours of temperature measured by profiling UAV interpolated from ascending and descending quadrotor aircraft (as described in Methods). Gaps between isocontours indicate times between flights. (b) Isocontours of potential temperature calculated from pressure and temperature as described in methods section. Vertical lines in (a) and (b) indicate boundaries between regimes with regimes identified by roman numerals in (a).

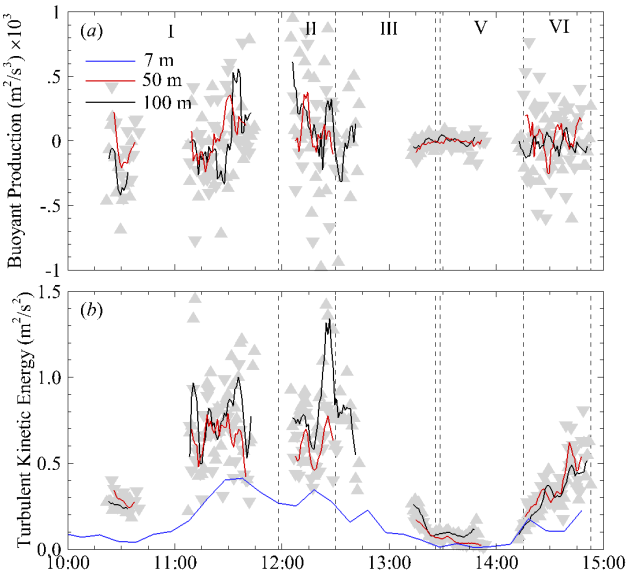

Figure 4: Time evolution of turbulence statistics measured at 7 m, 50 m and 100 m: (a) Buoyant production calculated from fixed wing aircraft flying at 50 m and 100 m; (b) Corresponding turbulent kinetic energy, compared to estimated turbulent kinetic energy measured by sonic anemometer located at 7 m. Vertical lines in (a) and (b) indicate boundaries between regimes with regimes identified by roman numerals in (a). Gray data points indicate statistics gathered from a single pass, with lines produced via a rolling average of 5 passes. Upward pointing triangles indicate a measurement made at 100 m and downward pointing triangles indicate a measurement made at 50 m.